CrossMark

Towards full-resolution inline electron holography☆

Christoph T. Koch *

Institute for Experimental Physics, Ulm University, 89081 Ulm, Germany

ARTICLE INFO

This work is dedicated to the memory of Prof. David J.H. Cockayne.

ABSTRACT

With the availability of fast computers, inline electron holography, a technique for reconstructing both amplitude and phase of the electron wave function as scattered by the sample from a set of differently aberrated transmission electron microscopy images, is becoming increasingly quantitative. While focal series reconstruction from transmission electron microscopy images has already been practiced for at least 3 decades, existing approaches can only recover a relatively small band of spatial frequencies. Here I present a reconstruction scheme which is capable of reconstructing the electron wave function for a very large range of spatial frequencies, demonstrating its performance using simulated as well as experimental data.

© 2013 The Author. Published by Elsevier Ltd. All rights reserved.

1. Introduction

In the field of transmission electron microscopy (TEM) the term 'electron holography' is typically synonymous with 'off-axis electron holography' performed by interfering different parts of a coherent electron wave function using an electrostatic biprism. However, in addition to being a much simpler experiment, it has been shown that inline holography, in its experimental setup much closer to Gabor's original idea (Gabor, 1948), can be just as quantitative (Latychevskaia et al., 2010), can achieve much better signal/noise properties for the same dose (Koch and Lubk, 2010), and measure holographic information also in cases where off-axis holography cannot be applied due to the absence of a suitable reference area (Özdöl et al., 2010).

As Gabor noted already very early on, reconstructing a general complex wave function from a single inline hologram, without making any additional assumptions about the scattering object, is an ill-posed problem, and the reconstruction is hampered by the so-called twin image problem. However, computer algorithms which are much more flexible than Gabor's original holographic reconstruction principle using laser light, can consider inline holograms recorded at multiple planes of focus and thus overdetermine the problem and solve the twin image problem.

Fig. 1 shows an example focal series that was simulated from a test object featuring both amplitude and phase contrast. For simplicity the absorption in this object has been set to be proportional to the phase shift it imposes on the penetrating fast electrons. This is why the focused image ($\Delta f = 0$) shows any contrast at all. Note that, in contrast to conventional focal series, the defocus varies in a non-linear fashion (Koch, 2012). The modulus of the defocus in this series obeys the following relation:

$$|\Delta f_n| = \Delta f |(n - n_{ref})^p| \tag{1}$$

where in this case, $p = 3$, $n_{ref} = 3$, $\Delta f = 200$ nm, and $n = 0, 1, \ldots, 6$. Reason for this non-linear defocus variation is the efficient sampling of high and low frequency information in the phase of the exit wave function. While at low absolute defocus, small variations in defocus produce a lot of change in image contrast, applying the same defocus change starting from some large under- or overfocus has, due to the partial spatial coherence of the illumination, hardly any effect on the image contrast at all. Efficiency in this context means the acquisition of only a few images while still transferring a large range of spatial frequencies with sufficient contrast, even in the presence of noise. The plot at the bottom left of Fig. 1 shows the two phase transfer functions.

$$PTF_{\Delta f = 5.4\,\mu m}(|\vec{q}|) = \text{Im}[CTF(|\vec{q}|, \Delta f = 5.4\,\mu m)] \cdot E_s(|\vec{q}|, \Delta f = 5.4\,\mu m)$$

$$PTF_{eff}(|\vec{q}|) = max[|\text{Im}[CTF(|\vec{q}|, \Delta f)]| \cdot E_s(|\vec{q}|, \Delta f)] \tag{2}$$

where the effective phase transfer function $PTF_{eff}(|\vec{q}|)$ is determined as the maximum of the absolute value of the imaginary parts of any of the $CTF(\vec{q})$ functions (see expression (3)) at the available defoci for a given spatial frequency $|\vec{q}|$. Both functions have also been multiplied by the objective aperture which limits the resolution in this case to 5 Å. As can be seen from this example, the
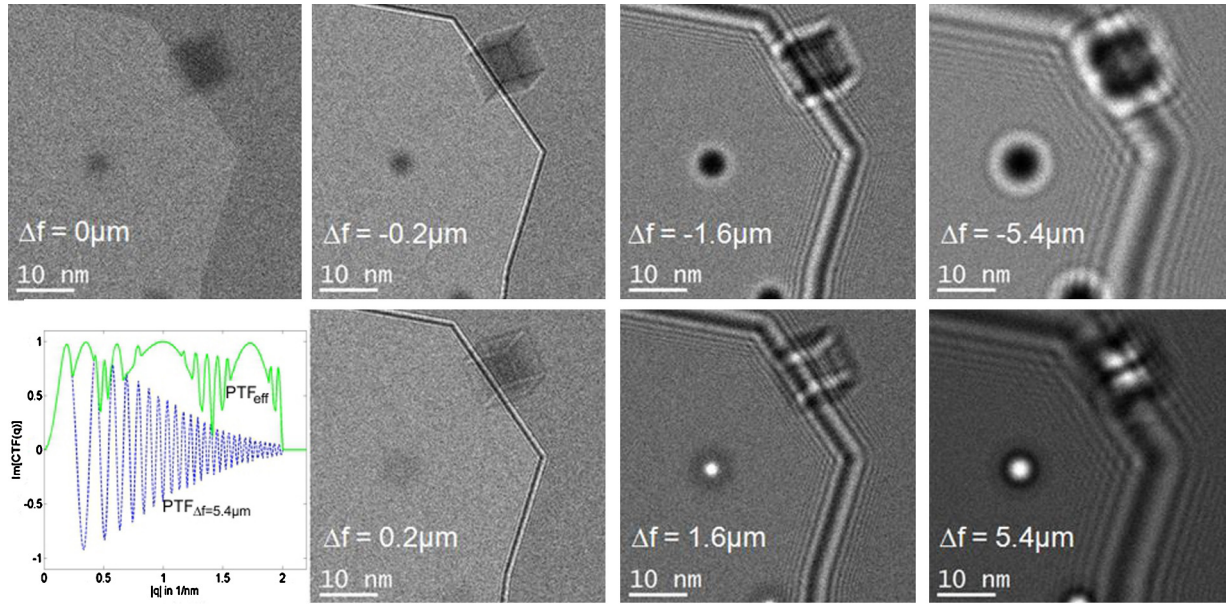
Fig. 1. Simulated 7-member focal series of TEM images of a test object featuring both amplitude and phase contrast. Simulation parameters: beam energy $E_0 = 200$ kV ($\lambda = 2.51$ pm), illumination semi-convergence angle $\alpha = 0.05$ mrad, spherical aberration coefficient $C_s = 1.0$ mm, focal spread $\Delta_f = 10$ nm, objective aperture admitting scattering angles up to $\theta_{max} = 5$ mrad, thus limiting the spatial resolution to 0.5 nm, pixel size 0.1 nm, dose in each image: 34.2 electrons per Å^2 (total dose of 240 electrons per Å^2, Poisson noise, contrast adjusted to intensity range). At the bottom left, the phase transfer function (PTF) corresponding to the largest defocus, as well, as the effective PTF for the complete series are shown (see expressions (2) and (3) for details).

large range of defocus values causes the PTF_{eff} function to exceed a value of 0.1 for a range of spatial frequencies between 0.05 nm^{-1} and 2 nm^{-1}. In principle, such large range of spatial frequencies could also be covered by a linearly spaced focal series with a defocus step of $d\Delta f = 1.8$ μm. However, correctly aligning images that differ by such a large amount of defocus is much more difficult (if at all possible) than aligning images with a much smaller difference in defocus. The algorithm presented below therefore first aligns only the images with very small absolute values of the defocus and then aligns images recorded at large defocus with those simulated for that defocus from the current estimate of the exit wave function. In principle, the choice of defocus values could be further optimized, including using non-equal pairs for over- and underfocus. However, such optimization (e.g. as described in Miedema et al. (1994) and Buist et al. (1996)) is beyond the scope of this work. We have already very successfully applied such non-linear focus variation for various bright-field and dark-field inline holography experiments (e.g. (Song et al., 2013)). More recently, Haigh et al. (2013) have also shown that extending the defocus range by combining two linear focal series with different defocus steps provides access to both high and low spatial frequencies.

The imaging model used within this work assumes, in its treatment of the partial spatial coherence, that the effect of partial spatial coherence is dominated by the oscillations in the coherent transfer function (CTF) due to first order aberrations, such as defocus or astigmatism. This is the case either in an aberration-corrected instrument, or in cases where a resolution-limiting objective aperture is in place, as is the case for the simulations and experiments presented in this work. According to Koch (2008) the image intensity $I(\vec{r})$, considering only defocus (Δf), astigmatism (amplitude A and direction ϕ_A), spherical aberration (C_s), partial temporal coherence characterized by the focal spread Δ_f, partial spatial coherence characterized by the illumination semi-convergence angle α, an objective aperture ($H(\vec{q})$) transferring scattering angles $\theta \leq \theta_{max}$,

and the modulation transfer function $MTF(q)$ of the detector, is given by

$$
\begin{aligned}
I(\vec{r}) &= FT^{-1}[I_\Delta(\vec{q}, \Delta f) \cdot E_s(\vec{q}, \Delta f) \cdot MTF(q)] \\
I_\Delta(\vec{r}) &= |FT^{-1}(\Psi(\vec{q}) \cdot CTF(q, \Delta f) \cdot E_\Delta(\vec{q}) \cdot H(\vec{q}))|^2 \\
CTF(\vec{q}) &= \exp(i\pi\lambda|\vec{q}|^2[\Delta f + A\cos(2[\phi - \phi_A]) + 0.5\lambda^2 C_s|\vec{q}|^2]) \\
E_\Delta(\vec{q}) &= \exp(-[0.5\pi\lambda\Delta_f|\vec{q}|^2]^2) \\
H(\vec{q}) &= \begin{cases} 1, & \lambda|\vec{q}| \leq \theta_{max} \\ 0, & \lambda|\vec{q}| > \theta_{max} \end{cases} \\
E_s(\vec{q}) &= \exp(-[\pi\alpha\{\Delta f + A\cos(2[\phi - \phi_A])\}|\vec{q}|]^2)
\end{aligned}
\tag{3}
$$

where $\vec{r}$ and $\vec{q}$ are 2-dimensional coordinates in real and reciprocal space, respectively, $\phi = \tan^{-1}(q_y/q_x)$, λ is the electron wavelength, and $\Psi(\vec{r})$ is the exit face wave function that is ultimately to be reconstructed.

There exist numerous algorithms to reconstruct the electron wave function from focal series, each making its own approximation (Allen and Oxley, 2001; Allen et al., 2004; Coene et al., 1996; Hsieh et al., 2004; Kawasaki et al., 2001; Kirkland, 1984; Kirkland et al., 1995; Koch, 2008; Morgan et al., 2011; Teague, 1983). While most iterative algorithms may reconstruct high-frequency details very nicely, they often require computationally prohibitive numbers of iterations (e.g. several 10^5 (Ophus and Ewalds, 2012)) to reconstruct low-frequency details. Deterministic phase retrieval algorithms (Kawasaki et al., 2001; Morgan et al., 2011; Op de Beek et al., 1996; Teague, 1983) usually make linear approximations and have other shortcomings, e.g. no mechanism to self-consistently verify the initial alignment of the experimental images, or, in the case of the transport-of-intensity equation (TIE) (Teague, 1983), the amplification of low-frequency noise for small defocus changes and missing high-frequency detail at larger defocus changes.
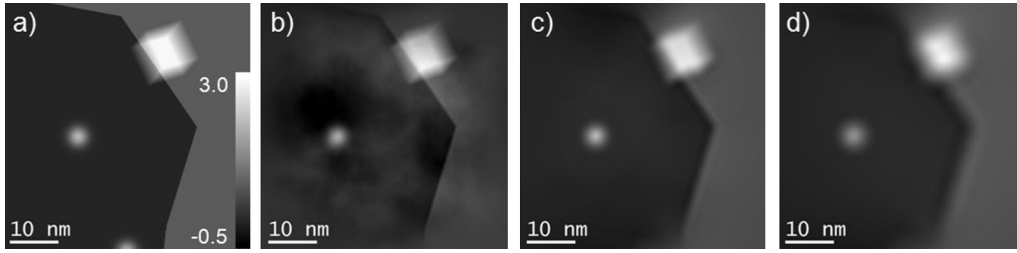
Fig. 2. Original (a) and TIE-reconstructed phase from 3-membered focal series with defocus values (b) −0.2 μm, 0, and 0.2 μm, (c) −1.6 μm, 0, 1.6 μm, and (d) −5.4 μm, 0, 5.4 μm. In order to make the total dose the same as in Fig. 1 the dose in each of the simulated images has been 80 electrons per Å^2 (total dose is thus 240 electrons per Å^2).

Fig. 2 shows how applying the TIE to ideal but noisy data may introduce low frequency artefacts in the reconstructed phase of the exit wave function. The reason for this lies in the mathematical expression employed by the TIE to determine the phase.

$$\frac{2\pi}{\lambda}\frac{\partial I(\vec{r}, \Delta f)}{\partial \Delta f} = \nabla_{x,y} \cdot [I(\vec{r}, \Delta f)\nabla_{x,y}\phi(\vec{r}, \Delta f)] \qquad (4)$$

where $I(\vec{r}, \Delta f)$ is the intensity at position $\vec{r}$ recorded with the defocus Δf, and $\phi(\vec{r}, \Delta f)$ is the phase of the aberrated wave function corresponding to that image. Typically, 3 images are recorded, one in focus ($\Delta f = 0$), one at overfocus, and another at underfocus, so that the defocus derivative $((\partial I(\vec{r}, \Delta f))/(\partial \Delta f))|_{\Delta f=0}$ can be approximated by finite difference (Ishizuka and Allman, 2005). For phase objects, i.e. wave functions with constant amplitude this expression reduces to the simple Poisson-like equation

$$\nabla^2_{x,y}\phi(\vec{r}) = \frac{2\pi}{I_0\lambda}\frac{\partial I(\vec{r})}{\partial \Delta f} \qquad (5)$$

Here we assumed the target defocus to be zero ($\Delta f = 0$) and I_0 is the constant intensity of that focused image. If the boundary conditions are known, then both expressions can, in principle be solved. Problems in electrostatics which solve the Poisson equation that is very similar to expression (5) often need to define either Dirichlet or Neumann boundary conditions. However, the problem in phase retrieval is that these boundary conditions are not known. In order to be able to determine the phase at all, periodic boundary conditions are commonly assumed (Paganin and Nugent, 1998). Also, both expressions (4) and (5) are low pass filters for noise when solving for the phase $\phi(\vec{r})$, and regularization to avoid divergence at very low spatial frequencies must be applied. This regularization is commonly implemented in form of a Tikhonov filter (Ishizuka and Allman, 2005).

As can be seen from Fig. 2, the defocus step used to compute $\partial I(\vec{r})/\partial \Delta f$ via the finite difference approximation shifts the band of spatial frequencies that are reconstructed well. A small defocus step will result in a good reconstruction at high spatial frequencies and amplification of noise at low frequencies and a large defocus step can reconstruct low spatial frequencies much better, but does a poor job at high spatial frequencies. At the same time the periodic (or similarly inaccurate) boundary conditions which must be assumed to solve for the phase in expression (4) produce artifacts near the edges of the area from which the phase shift is reconstructed. It has been shown that iterative reconstruction schemes may reconstruct the phase from 3 images without assuming some boundary condition (Allen and Oxley, 2001), but the robustness of the reconstruction against noise and the ability to recover accurate phase information across a very wide range of spatial frequencies are improved when recording more than 3 images, spanning a wide range of defocus values (Buist et al., 1996). It shall be clarified here that within the scope of this manuscript 'full resolution' is considered relative to the information limit within and the field of view of the image, and not on some absolute scale.

2. The FRIH reconstruction algorithm

The approach to full-resolution inline holography (FRIH) presented here is based on combining the advantages of iterative focal series reconstruction algorithms, more specifically the flux-preserving variant (Koch, 2008) with the capability of the TIE to predict relative phases across large distances. An obvious choice of combining a solution to the TIE with iterative phase retrieval might be to refine an initial guess for the wave function obtained by the TIE using the iterative algorithm which adjusts predominantly the high spatial frequencies (Gureyev, 2003), in some way similar also to the well-known PAM-MAL approach which refines an initial phase estimate obtained by the parabola method (PAM) using a maximum likelihood (MAL) algorithm (Thust et al., 1996).

However, such an algorithm would not avoid artifacts due to periodic boundary conditions, and, more importantly, we would still have the problem of potentially amplifying noise at low spatial frequencies. The regularization parameter for the initial TIE estimate would have to be defined beforehand, and, since this parameter will always have to be a trade-off between recovering low frequency phase information and amplifying noise, there is no obvious choice. A more practical problem is the image registration for doing the TIE reconstruction. Images acquired at different defocus have different contrast, and can therefore not easily be aligned in an automated fashion using cross-correlation or similar approaches. This problem becomes even more severe if one considers the relative distortions of images acquired with different defocus. Several attempts I have made to implement such an approach have failed and proved not to be reliable at all.

An iterative algorithm, such as the flux-preserving reconstruction algorithm (FPRA) described earlier (Koch, 2008) has the opportunity to adjust, between iterations of the actual wave reconstruction, the image registration between images simulated from the current estimate of the wave function, and the corresponding experimental ones. The initial image alignment is therefore not as critical for the final result, as it is for a deterministic approach, since the alignment can be improved self-consistently during reconstruction, an option not available with the TIE, for example.

The approach to inline electron holography presented here aims at reconstructing as large as possible a bandwidth of spatial frequencies and is based on the flux-preserving reconstruction algorithm (Koch, 2008), adding the following improvements:

1 *Large defocus range*: The confidence with which low spatial frequency information in the phase can be recovered depends both on the spatial coherence of the illumination, and also on how large the range of defocus values for which images are acquired, is Op de Beek et al. (1996).
2 *Non-linear sampling of defocus values*: The obvious reason is that, due to partial spatial coherence, the same small defocus step necessary to capture high-frequency phase information near optimum defocus produces almost no change in contrast at the large defocus values necessary to recover low-frequency
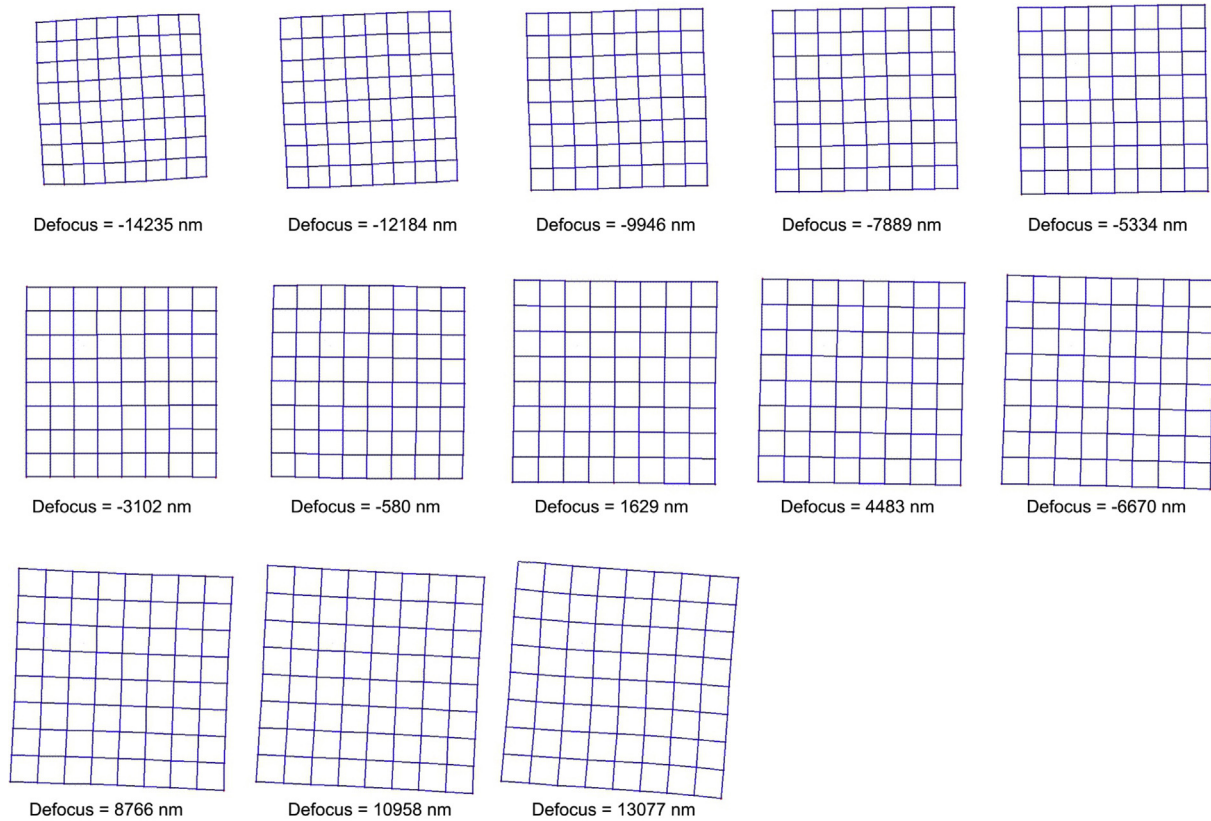
Fig. 3. Distortions of an example focal series for a Zeiss Libra 200 MC amplified 5-fold. These distortions have been measured and self-consistently corrected during phase reconstruction with the flux-preserving reconstruction algorithm (FPRA) (Koch, 2008).

information as can be seen, for example, in Fig. 1. Since there is no need to have uniform sampling of defocus, this algorithm and the automated acquisition software that has been developed for it (see Fig. 5) allows the defocus to be varied non uniformly, e.g. according to expression (1).

3 *Incremental inclusion of images*: Looking at Fig. 1 it becomes obvious that images with largely different defocus cannot easily be aligned. However, starting the reconstruction with only slightly defocused images (e.g. $\Delta f = -200$ nm, 0, and +200 nm) and then aligning the next larger defocus values (in the example of Fig. 1 $\Delta f = \pm 1.6 \, \mu$m) with images simulated from the current estimate of the wave function, based on only 3 images, works very reliably. Repeating this approach will ultimately include all frames of the focal series, but guarantees a highly accurate alignment, even if the images are strongly defocused.

4 *Distortion correction*: Changing the defocus by adjusting the current running through the objective lens will also affect the magnification, rotation of the image, and to some degree also distortions of the images (see, for example, Fig. 3). An iterative reconstruction algorithm can in most cases include a refinement of the changes in the image geometry every few iterations. Such automated distortion measurement and compensation has been implemented in the algorithm described here.

5 *Padding*: Reconstructing a wave function that is larger than the experimental images, or the sub-area in the experimental image stack selected for reconstruction has been shown by Ophus and Ewalds (2012) to help in the reconstruction of low spatial frequency phase information, because it relaxes the otherwise very stringent periodic boundary conditions.

6 *Phase prediction*: As mentioned earlier, iterative projection (Allen and Oxley, 2001; Allen et al., 2004; Koch, 2008) and gradient descent (Coene et al., 1996; Hsieh et al., 2004; Kirkland, 1984)

phase reconstruction algorithms have the property that they reconstruct high spatial frequency information in the phase first and do a poor job in reconstructing low spatial frequencies. In order to overcome this limitation the FRIH algorithm includes iterations which apply a TIE-like approach as explained below to make the phase converge much faster. However, this phase prediction is done in a very conservative manner in that large changes in the phase in individual iterations are suppressed. Also, at low spatial frequencies, phase shifts predicted from more strongly defocused images are given more weight. This preserves the self-consistency and well-behaved convergence of iterative reconstruction algorithms, but improves the speed of convergence dramatically, especially for low spatial frequencies (see Figs. 4 and 7).

Fig. 4 shows the comparison of amplitudes and phases reconstructed by different iterative approaches. The FPRA algorithm used to reconstruct the wave function shown in Fig. 4a already includes improvements 1–4 in the above list. Adding the next item in the list, padding, improves the phase for features near the edges of the reconstructed area (see the FPRA + padding (FPRAP) reconstruction in Fig. 4b). The most dramatic improvement, however, is due to the last item in the above list, phase prediction, which is why this approach is given a different name, full-resolution inline holography (FRIH), because this approach is able to reconstruct both high and low frequency details in the phase very accurately, as can be seen when comparing Fig. 4c to the original phase in Fig. 4d.

As mentioned above, phase prediction works by applying a TIE-like approach, i.e. solve expression (4) with the modification that

$$\frac{\partial I(\vec{r}, \Delta f)}{\partial \Delta f} \Leftarrow \frac{I_{exp}(\vec{r}, \Delta f) - I_{sim}(\vec{r}, \Delta f)}{\Delta f} \qquad (6)$$
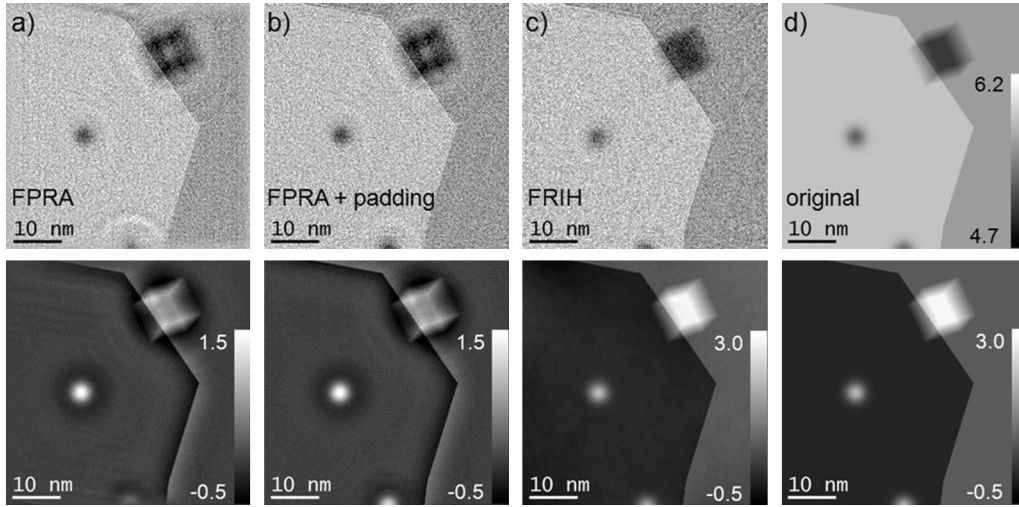
Fig. 4. Comparison of different reconstruction algorithm: Amplitude (top) and phase (bottom) for (a) the flux-preserving reconstruction algorithm (FRPA), (b) FRPA while padding the images with 25% of the image size at each edge, (c) full-resolution inline holography (FRIH) reconstruction algorithm, and (d) the original wave function. The same number of iterations was applied for all 3 algorithm variants (6 iterations with 3 images + 6 iterations with 5 images + 6 iterations with 7 images + 20 final iterations with all 7 images).

i.e. the intensity variation with defocus $\partial I(\vec{r}, \Delta f)/\partial \Delta f$ is replaced with the reconstruction residual, the difference between the experimental image intensities $I_{exp}(\vec{r}, \Delta f)$ and the ones computed from the current estimate of the reconstructed wave function, $I_{sim}(\vec{r}, \Delta f)$, divided by the defocus Δf at which the image has been acquired. This will only predict any phase change as long as the reconstruction has not converged yet. Since the solution to Eq. (4) can predict very large changes in the phase, the FRIH algorithm accepts only changes in the phase up to an adjustable maximum. Setting this maximum to about 0.1 rad works very well.

3. Results and discussion

Having shown that the FRIH algorithm works well on simulated data we can now test it on experimental data. The test data set is a zero-loss filtered focal series acquired on the 200 kV Zeiss SESAM FEG-TEM (Koch et al., 2006). The focal series is comprised of 15 images spanning the range of defocus values of $-11.5\,\mu$m to $+10.0\,\mu$m in linear defocus increments. The test sample is a CeO_2 ceramic thinned by mechanical wedge polishing. Strong phase variations due to different orientations of the grains, thickness fringes, grain boundaries, and also overlapping grains are expected. The focal series has been acquired on a Gatan Orius 1000 CCD camera with a defocus step of 1.63 μm. The precise defocus values have been refined during reconstruction. After a rough pre-alignment an area of 1380×1510 pixels has been selected for the reconstruction. The size of the padded wave function was set to be 1.5 times larger than the selected area, i.e. 2070×2265 pixels.

Fig. 6 shows a comparison of phases and amplitudes of the wave functions reconstructed by both the FPRAP and the FRIH algorithms. While the FPRAP algorithm converges very slowly, the FRIH algorithm has reconstructed the low-frequency phase information already after comparatively few iterations. In fact, in most cases no more than 20 final iterations are needed for convergence. However, I have decided to show the result after 100 iterations to demonstrate that the solution remained sane and did not diverge after many more iterations than necessary.

Table 1 shows that the better reconstruction of low-frequency phase information is also reflected in the commonly used convergence criteria, the residual R and the normalized sum of squared differences χ^2 which are defined as

$$R = \frac{\sum_{\Delta f} \sum_{r} |I_{sim}(\vec{r}, \Delta f) - I_{exp}(\vec{r}, \Delta f)|}{\sum_{\Delta f} \sum_{r} |I_{exp}(\vec{r}, \Delta f)|} \tag{7}$$
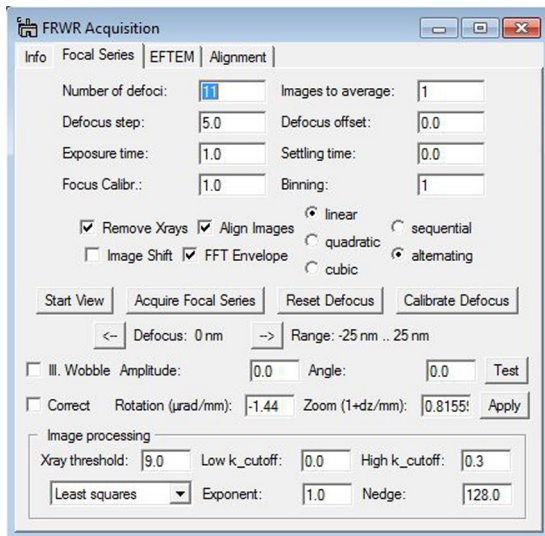

Fig. 5. Screen shot of the graphical user interface used to collect drift-corrected focal series with linear ($p = 1$), quadratic ($p = 2$), or cubic ($p = 3$) defocus increments. The drift correction allows multiple images at the same defocus to be acquired. These images are then averaged after removing X-ray hits and aligning them, using either cross correlation, or (preferably) a squared difference map. This plugin to the Gatan DigitalMicrograph software (Gatan Inc., Pleasanton, CA, USA), which also contains a long menu of functions not included in this GUI can be freely downloaded from the web.
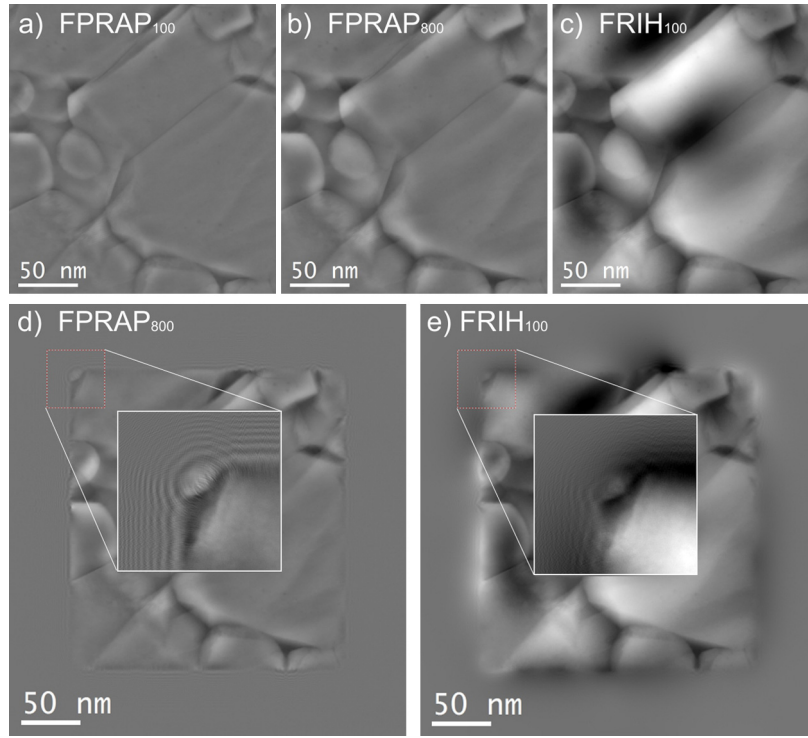
Table 1
Comparison of the convergence of the original and modified FPRAP algorithm. Two figures of merit, the normalized χ^2 and the R-value defined in expressions (7) and (8) are given. This comparison shows that the FRIH algorithm converges to a good solution much faster.

FPRAP, $N_{iter} = 100$	FPRAP, $N_{iter} = 800$	FRIH, $N_{iter} = 100$
$\chi^2 = 0.61\%$	$\chi^2 = 0.44\%$	$\chi^2 = 0.42\%$
$R = 4.94\%$	$R = 4.32\%$	$R = 4.11\%$

Fig. 6. Phase maps (1380 × 1510 pixels) reconstructed from a 15-member focal series of a CeO$_2$ ceramic by FPRAP and FRIH. FPRAP results are shown after 100 (a) and after 800 (b) iterations. The FRIH result (c) is shown after 100 iterations. (d) and (e) the results shown in (b) and (c), but including the padded region for which no experimental data was available. The gray scales of figures (a)–(e) have been set to span the range of −3.9 to 4.7 rad. The gray scale of the insets showing how the phase extends into the padded region in (d) and (e) has been adjusted to cover the range of −1.2 to 1.6 rad.

$$\chi^2 = \frac{\sum_{\Delta f}\sum_r (I_{sim}(\vec{r}, \Delta f) - I_{exp}(\vec{r}, \Delta f))^2}{\sum_{\Delta f}\sum_r (I_{exp}(\vec{r}, \Delta f))^2} \qquad (8)$$

where $I_{exp}(\vec{r}, \Delta f)$ are the experimental image intensities at positions $\vec{r}$ in the image acquired with defocus Δf and $I_{sim}(\vec{r}, \Delta f)$ the corresponding image intensities simulated from the reconstructed wave function at those positions for the same defocus. In each of these cases the comparison thus includes all pixels in all frames of the focal series.

To better compare the convergence of these algorithms, Fig. 7 compares the *R*-value as function of iteration for both the FPRAP and FRIH algorithms. This plot very nicely shows that the FRIH algorithm has already converged after just a few iterations, not counting the alignment iterations that do not include all the images of the focal series yet. Starting with the 9th, 10th, and 11th frame of the focal series 9 iterations have been computed before including more images in the reconstruction. This is why the R-value features sharp increases every 9 iterations before dropping again. In the case of the FRIH algorithm these 9 alignment iterations have been split up into 4 normal FPRAP iterations, followed by 5 FRIH iterations including also phase prediction. This explains the abrupt changes in slopes of the convergence curve in the middle of the 9 alignment loops.

Having presented a comparison between FRIH and a more or less conventional iterative reconstruction algorithm, Fig. 8 compares the FRIH result with 3-image TIE reconstructions for different defocus steps, very similar to Fig. 2, but this time for experimental data. The images used for the TIE reconstructions have been corrected for drift and image distortions using the FPRAP algorithm. Note that, since 3-image TIE is not self-consistent, the quality of the result depends very much on accurate pre-alignment of the images, which is difficult at large defocus, since these 3 images may have very different contrast. Using accurately aligned images the TIE

reconstruction is thus at least free from misalignment artifacts, so that one may more easily judge on the TIE-inherent reconstruction artifacts. This comparison shows that even at the smallest defocus step the spatial resolution is much worse than that of the FRIH reconstruction, and phase shifts in the TIE reconstructions seem to be continuous across grains, despite their often very different orientation and thickness.
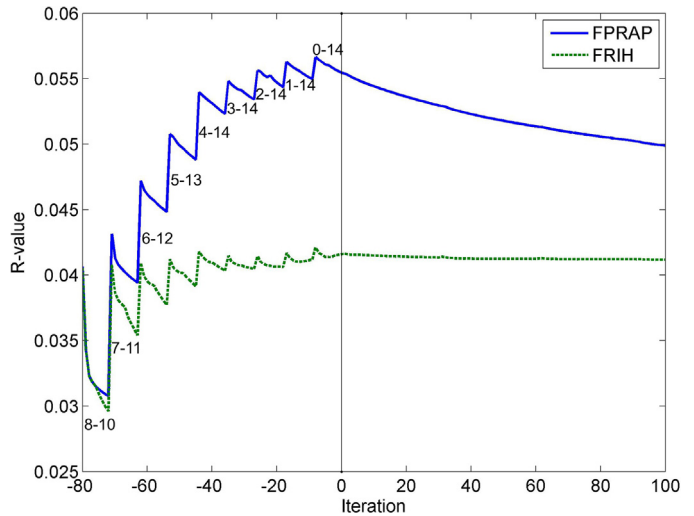

Fig. 7. *R*-value vs. iteration number for the FPRAP and FRIH algorithms. Negative iteration numbers mean that not all images have been included in the reconstruction yet. The range of frames (indices 0 . . . 14) included in the reconstruction at any time is indicated in the plot.
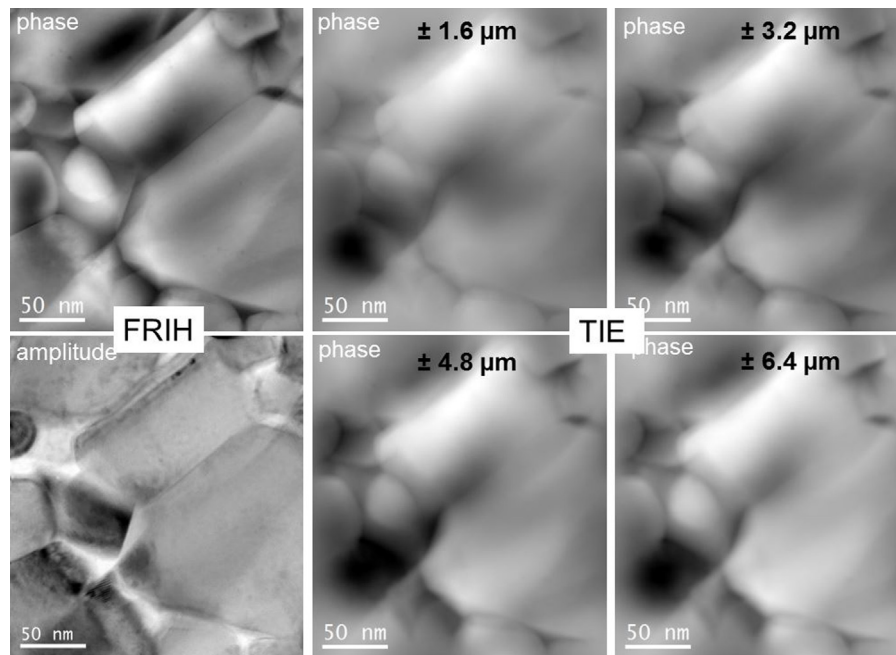
Fig. 8. Comparison of the phase of the exit wave function reconstructed using the FRIH algorithm, with TIE reconstructions for different pairs of defocused images. Four different pairs of defocus $-\Delta f$ and $+\Delta f$ ($\Delta f = 1.6\,\mu m$, 3.2 μm, 4.8 μm, and 6.4 μm) have been used to compute $\partial I(\vec{r})/\partial \Delta f$ in expression (4). The alignment and distortion correction of the defocused images as determined by the iterative reconstruction algorithms have been used.

4. Conclusion

This paper presents a novel approach to reconstruct the complex wave function from differently defocused TEM images (inline holograms) which can reconstruct simultaneously high and low spatial frequency information (full resolution) in the phase with only a few iterations. The improvement in the low-frequencies of the phase is achieved by applying a TIE-like approach to the difference of the experimental image intensities and the corresponding intensities simulated from the current estimate of the exit face wave function.

A fully automated reconstruction software implementing the full-resolution inline holography (FRIH) algorithm described in this paper has been developed, which includes the refinement of image alignment and image distortions in the reconstruction. Application of this approach to experimental bright-field (potential mapping) and dark-field (for strain mapping) inline holography has already delivered excellent results (e.g. Song et al. (2013)).

Acknowledgement

References

Özdöl, V.B., Koch, C.T., van Aken, P.A., 2010. A nondamaging electron microscopy approach to map In distribution in InGaN light-emitting diodes. J. Appl. Phys. 108, 056103.

Allen, L.J., Oxley, M.P., 2001. Phase retrieval from series of images obtained by defocus variation. Opt. Commun. 199, 65–75.

Allen, L.J., McBride, W., O'Leary, N.L., Oxley, M.P., 2004. Exit wave reconstruction at atomic resolution. Ultramicroscopy 100, 91–104.

Buist, A.H., van den Bos, A., Miedema, M.A.O., 1996. Optimal experimental design for exit wave reconstruction from focal series in tem. Ultramicroscopy 64, 137–152.

Coene, W.M.J., Thust, A., Op de Beek, M., Van Dyck, D., 1996. Maximum-likelihood method for focus-variation image reconstruction in high resolution transmission electron microscopy. Ultramicroscopy 64, 109–135.

Gabor, D., 1948. A new microscopic principle. Nature 161, 777–778.

Gureyev, T.E., 2003. Composite techniques for phase retrieval in the fresnel region. Opt. Commun. 220, 49–58.

Haigh, S.J., Jiang, B., Alloyeau, D., Kisielowski, C., Kirkland, A.I., 2013. Recording low and high spatial frequencies in exit wave reconstructions. Ultramicroscopy 133, 26–34.

Hsieh, W.-K., Chen, F.-R., Kai, J.-J., Kirkland, A.I., 2004. Resolution extension and exit wave reconstruction in complex HREM. Ultramicroscopy 98, 99–114.

Ishizuka, K., Allman, B., 2005. Phase measurement of atomic resolution image using transport of intensity equation. J. Electr. Microsc. 54, 191–197.

Kawasaki, T., Takai, Y., Ikuta, T., Shimizu, R., 2001. Wave field restoration using three-dimensional Fourier filtering method. Ultramicroscopy 90, 47–59.

Kirkland, A.I., Saxton, W.O., Chau, K.L., Tsuno, K., Kawasaki, M., 1995. Super-resolution by aperture synthesis: tilt series reconstruction in ctem. Ultramicroscopy 57, 355–374.

Kirkland, E.J., 1984. Improved high resolution image processing of bright field electron micrographs. Ultramicroscopy 15, 151–172.

Koch, C.T., Lubk, A., 2010. Off-axis and inline electron holography: a quantitative comparison. Ultramicroscopy 110, 460–471.

Koch, C.T., Sigle, W., Höschen, R., Rühle, M., Essers, E., Benner, G., Matijevic, M., 2006. Sesam: exploring the frontiers of electron microscopy. Microsc. Microanal. 12, 506–514.

Koch, C.T., 2008. A flux-preserving inline electron holography reconstruction algorithm for illumination of partial spatial coherence. Ultramicroscopy 108, 141–150.

Koch, C.T., 2012. Full-resolution inline electron holography (frih). In: European Microscopy Congress EMC2012, Manchester, UK, p. 139.

Latychevskaia, T., Formanek, P., Koch, C.T., Lubk, A., 2010. Off-axis and inline electron holography: experimental comparison. Ultramicroscopy 110, 472–482.

Miedema, M.A.O., van den Bos, A., Buist, A.H., 1994. Experimental design of exit wave reconstruction from a transmission electron microscope defocus series. IEEE Trans. Instrum. Meas. 43, 181–186.

Morgan, A.J., Martin, A.V., D'Alfonso, A.J., Putkunz, C.T., Allen, L.J., 2011. Direct exit-wave reconstruction from a single defocused image. Ultramicroscopy 111, 1455–1460.

Op de Beek, M., van Dyck, D., Coene, W.M.J., 1996. Wave function reconstruction in HRTEM: the parabola method. Ultramicroscopy 64, 167–183.

Ophus, C., Ewalds, T., 2012. Guidelines for quantitative reconstruction of complex exit waves in hrtem. Ultramicroscopy 113, 88.

Paganin, D., Nugent, K.A., 1998. Noninterferometric phase imaging with partially coherent light. Phys. Rev. Lett. 80, 2586–2589.

Song, K., Shin, G.Y., Kim, J.K., Oh, S.H., Koch, C.T., 2013. Strain mapping of led devices by dark-field inline electron holography: comparison between deterministic and iterative phase retrieval approaches. Ultramicroscopy 127, 119–125.

Teague, M., 1983. Deterministic phase retrieval: a green's function solution. J. Opt. Soc. Am. 73, 1434–1441.

Thust, A., Coene, W.M.J., Op de Beek, M., van Dyck, D., 1996. Focal-series reconstruction in hrtem: simulation studies on non-periodic objects. Ultramicroscopy 64, 211–230.